J. Fluid Mech. (2024), *vol*. 1000, A43, doi:10.1017/jfm.2024.986

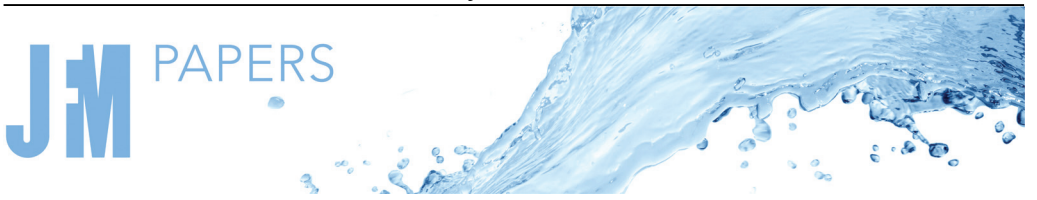

Ordinal pattern-based analysis of an opposition-controlled turbulent channel flow

Ryo Iseki[1], **Hiroshi Gotoda**[1] **and Yusuke Nabae**[1],†

[1]Department of Mechanical Engineering, Tokyo University of Science, 6-3-1 Niijuku, Katsushika-ku, Tokyo 125-8585, Japan

(Received 4 April 2024; revised 1 October 2024; accepted 9 October 2024)

We conduct a numerical study on the drag-reduction mechanism of an opposition-controlled turbulent channel flow from the viewpoint of a symbolic dynamics approach. The effect of the virtual wall formed by the opposition control is maximised at the location of the detection plane $y_d^+ \approx 10$. At this wall-normal location, the local link strength of the self-loop of network nodes representing the negative correlation pattern between the streamwise and wall-normal velocity fluctuations is maximised in the uncontrolled flow. In the controlled case, the multiscale complexity–entropy causality plane and the spatial permutation entropy at $y_d^+ \approx 10$ indicate that the drag-reduction effect is attributed to the reduction of the region where streaks actively coalesce and separate and the suppression of the regeneration cycle in the region near the wall.

Key words: drag reduction, turbulence control, channel flow

1. Introduction

Since turbulent motions significantly enhance skin friction drag compared with the corresponding laminar flow, skin friction drag reduction is of great importance for energy saving. Among numerous flow control methods for friction drag reduction (Kim 2003; Kasagi, Suzuki & Fukagata 2009; Ricco, Skote & Leschziner 2021; Fukagata, Iwamoto & Hasegawa 2024), the opposition control proposed by Choi, Moin & Kim (1994) is the simplest feedback control method. In this control method, a detection plane parallel to the wall is placed in the flow field, and the wall-normal velocity opposite to that detected on the detection plane is imposed on the wall. Choi *et al.* (1994) and Hammond, Bewley & Moin (1998) achieved a friction drag reduction of about 25 % in a low-Reynolds-number turbulent channel flow by direct numerical simulation (DNS). According to Hammond *et al.* (1998), the formation of the virtual wall in the fluid halfway between the physical wall and the detection plane, in which the wall-normal velocity fluctuations are approximately

† Email address for correspondence: yusuke.nabae@rs.tus.ac.jp

zero, results in the suppression of the momentum transport in the wall-normal direction, leading to a large drag-reduction effect. However, the details of the drag-reduction mechanism such as the effects of the virtual wall and turbulent energy transport in the opposition-controlled flow are still under investigation.

Nonlinear dynamical systems have provided a firm platform for dealing with diverse dynamical states: intermittency and deterministic chaos appearing in various aperiodic flow convections related to wall turbulence (Aubry *et al.* 1988; Sanghi & Aubry 1993; Holmes, Lumley & Berkooz 1996; Waleffe 1997; Eckhardt & Mersmann 1999; Moehlis, Faisst & Eckhardt 2004; Cavalieri 2021; Cavalieri & Nogueira 2022; Cavalieri, Rempel & Nogueira 2022). The strange attractor in dynamical systems exhibits an impressive geometrical pattern structure in a phase space. In the context of dynamical systems and information theory, the pattern of trajectories in a phase space can be linked to a finite string of symbolics (Amigó 2010). Ordinal patterns, which are defined by the rank order relations among continuous points of trajectories, are the Markov partition-based symbolic string representations that enable the unravelling of the structure of a phase space (Amigó 2010). The importance of ordinal patterns was first shown by Bandt & Pompe (2002) in their seminal and foundational works on permutation entropy (PE). Their works have paved a new way to the construction of a system for contemporary ordinal pattern-based analysis in the fields of mathematical science and related nonlinear physics. There are various useful methods that are of fundamental importance for evaluating the dynamical complexity, involving the PE (Bandt & Pompe 2002), the forbidden pattern number (Kulp & Zunino 2014; McCullough *et al.* 2016), symbolic recurrence plots (Marwan *et al.* 2007; Caballero-Pintado, Matilla-Garcia & Marin 2018) and the complexity–entropy causality plane (CECP) (Rosso *et al.* 2007). The PE is the information entropy of the symbols representing the rank-order patterns encoded from a time series and is the most well-used metric capable of quantifying the randomness of dynamic behaviour. The CECP is a two-dimensional plane consisting of the PE and Jensen–Shannon complexity to quantify the complexity of dynamic behaviour. The multiscale CECP (Zunino, Soriano & Rosso 2012) considering the embedding delay time in a phase space has shown to be an effective method for distinguishing between chaos and the stochastic process. These methods have enabled appropriate characterisation encompassing the understanding of the dynamical states appearing in a broad range of fluid phenomena: laminar–turbulent transition in a boundary layer flow (Li & Zuntao 2014; Zhang *et al.* 2017*b*), laboratory-scale plasmas and solar wind (Weck *et al.* 2015), falling liquid films (Gotoda, Pradas & Kalliadasis 2017*b*), a turbulent coaxial jet (Kobayashi *et al.* 2019) and a turbulent channel flow (Mamori *et al.* 2023). One of the present authors (Hayashi, Gotoda & Gentili 2016; Gotoda, Kobayashi & Hayashi 2017*a*; Takagi *et al.* 2017; Murayama *et al.* 2018; Nomi *et al.* 2021) has highlighted the applicability of ordinal pattern-based analysis to chemically reacting flow systems.

The substantial progress of network science originating from graph theory has led to diverse complex networks: the visibility graph (Lacasa *et al.* 2008), a correlation network (Gao & Jin 2009), the cycle network (Zhang & Small 2006), the recurrence network (Marwan *et al.* 2007) and the turbulence network (Taira, Nair & Brunton 2016). The complex-network approach has established a promising platform of analytical methods to expand our understanding of spatiotemporal dynamics in various turbulent flows (Gao & Jin 2009; Lozano-Durán & Jiménez 2014; Taira *et al.* 2016; Gotoda *et al.* 2017*b*; Iacobello *et al.* 2018; Kobayashi *et al.* 2019; Bae & Lee 2021; Chowdhuri, Iacobello & Banerjee 2021; Iacobello, Ridolfi & Scarsoglio 2021; De *et al.* 2023; Mamori *et al.* 2023). Along the line of the concept of symbolic dynamics, Small and co-workers (Small 2013; McCullough *et al.* 2015) proposed the ordinal partition transition network (OPTN)

as a specific type of transition network. Mamori *et al.* (2023) have recently shown that the univariate OPTN entropy is useful for assessing the randomness of the streamwise velocity in a turbulent channel flow. They also clarified the formation of a low-dimensional (high-dimensional) chaotic state of the streamwise velocity fluctuations at a viscous sublayer (logarithmic layer). This recent study by Mamori *et al.* (2023) has importantly brought about a foothold for the interdisciplinary fusion between symbolic and turbulent dynamics. One of our primary interests and motivations in this study is to extend our understanding of the drag-reduction mechanism on controlled turbulent channel flow by clarifying the physical link between the symbolic dynamics-based complexity metrics and the spatiotemporal structure of uncontrolled/controlled turbulent channel flow. This challenging subject still remains unexplored over a long period of wall-turbulent flow research. In fact, notwithstanding the many uncontrolled/controlled wall-turbulent flow studies (Kim 2003; Kasagi *et al.* 2009; Ricco *et al.* 2021; Fukagata *et al.* 2024) using DNS, the details of the drag-reduction mechanism of the opposition-controlled flow have not been investigated even under a low-Reynolds-number condition from the viewpoint of the symbolic dynamics approach.

On the basis of the above background, the main objective of this study is to investigate the drag-reduction mechanism of an opposition-controlled turbulent channel flow by ordinal pattern-based analysis, with a particular focus on the effect of the virtual wall. In this study, we consider the multivariate OPTN (Zhang *et al.* 2017*a*), multiscale CECP, and spatial permutation entropy (SPE) (Zunino & Ribeiro 2016). The rest of the paper is organised into four sections. In §§ 2 and 3, we explain the basic framework of DNS and ordinal pattern-based analysis, respectively. In § 4, we present the drag-reduction mechanism, showing the applicability of ordinal pattern based-analysis to the appropriate control of a turbulent channel flow. We provide a summary in § 5.

2. Direct numerical simulation

The governing equations are the incompressible continuity and Navier–Stokes equations, i.e.

$$\frac{\partial u_i}{\partial x_i} = 0, \tag{2.1}$$

$$\frac{\partial u_i}{\partial t} = -\frac{\partial (u_i u_j)}{\partial x_j} - \frac{\partial p}{\partial x_i} + \frac{1}{Re_\tau}\frac{\partial^2 u_i}{\partial x_j \partial x_j} - \frac{\mathrm{d}P}{\mathrm{d}x_1}\delta_{i1}, \tag{2.2}$$

where u_i $(i = 1, 2, 3)$ and p denote the velocity components and pressure, respectively. Moreover, 1, 2 and 3 denote the streamwise, wall-normal and spanwise directions, respectively. All variables are made dimensionless by the friction velocity u_τ^*, channel half-width δ^* and fluid density ρ^*, where the superscript $*$ denotes dimensional quantities. We perform all simulations under a constant pressure gradient (CPG) condition at $Re_\tau = u_\tau^* \delta^* / \nu^* = 180$ and 590, where ν^* is the kinematic viscosity. The computational conditions in the present DNS are summarised in table 1, where L_i, N_i and Δx_i denote the computational domain, the number of grid points and the grid spacing, respectively, in the ith direction, and Δt is the time resolution of DNS. Note that the superscript + represents wall units non-dimensionalised by the friction velocity and kinematic viscosity.

The DNS code used in this study is based on that developed by Fukagata, Kasagi & Koumoutsakos (2006) and extended by Nabae & Fukagata (2024). The governing equations are spatially discretised using the energy-conserving fourth-order finite-difference scheme (Morinishi *et al.* 1998) in the streamwise and spanwise directions

Re_τ	$L_1 \times L_2 \times L_3$	$N_1 \times N_2 \times N_3$	Δx_1^+	Δx_2^+	Δx_3^+	Δt^+
180	$4\pi \times 2 \times 2\pi$	$256 \times 96 \times 256$	8.8	0.9–6.0	4.4	0.036
590	$2\pi \times 2 \times \pi$	$384 \times 256 \times 384$	9.7	0.9–7.6	4.8	0.036

Table 1. Computational conditions in the present DNS.

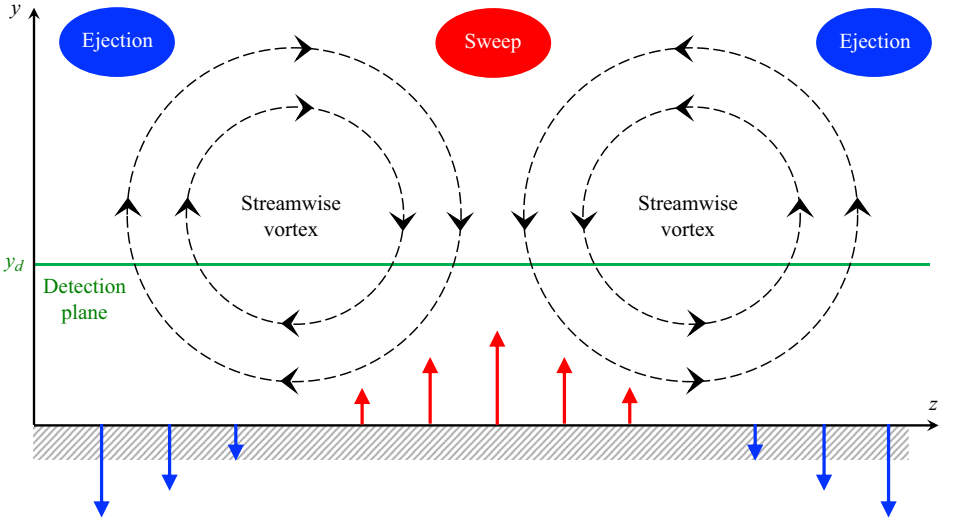

Figure 1. Schematic of opposition control.

and the second-order finite-difference scheme in the wall-normal direction. The time integration is conducted using the low-storage third-order Runge–Kutta/Crank–Nicolson scheme (Spalart, Moser & Rogers 1991) with the higher-order simplified marker and cell (SMAC)-like velocity–pressure coupling scheme (Dukowicz & Dvinsky 1992). The pressure Poisson equation is solved by the fast Fourier transformation in the streamwise and spanwise directions and the tridiagonal matrix algorithm in the wall-normal direction.

We apply the periodic boundary condition in the streamwise and spanwise directions. The boundary conditions for the streamwise and spanwise velocities on the walls are $u = 0$ and $w = 0$, respectively. In addition, the boundary conditions for the wall-normal velocity on the walls in the uncontrolled and controlled cases are $v = 0$ and

$$\left.\begin{array}{l} v(y=0) = -v(y=y_d) \quad \text{(lower wall)}, \\ v(y=2) = -v(y=2-y_d) \quad \text{(upper wall)}, \end{array}\right\} \tag{2.3}$$

respectively, where y_d denotes the location of the detection plane shown in figure 1. In this study, we set five different detection planes, i.e. $y_d^+ \approx 5$, 7.5, 10, 15 and 20.

The drag-reduction rate R_D is defined as

$$R_D = 1 - \frac{C_f}{C_{f0}}, \tag{2.4}$$

where C_f and C_{f0} are the drag coefficients in the controlled and uncontrolled cases, respectively. These drag coefficients are calculated as $C_f = 1/U_b^{+2}$ and $C_{f0} = 1/U_{b,NC}^{+\,2}$, respectively. Here, $U_{b,NC}^+$ is the bulk-mean velocity in the uncontrolled case. Similarly to

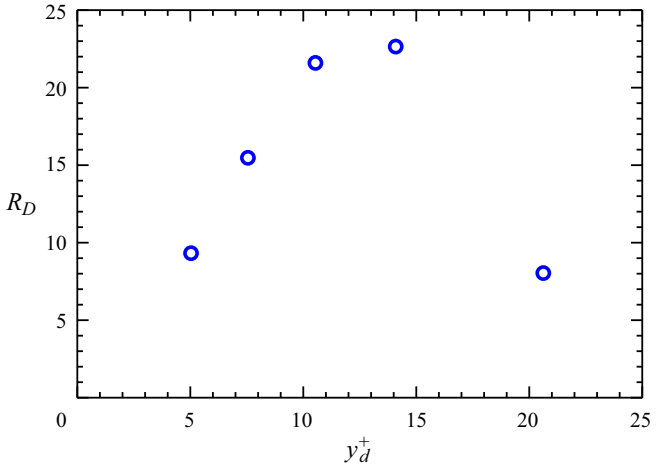

Figure 2. Drag-reduction rates at different y_d^+ values in all cases.

Nabae, Kawai & Fukagata (2020), $U_{b,NC}^+$ is calculated using the approximation formula proposed by Nabae *et al.* (2020) regarding the relationship between the bulk Reynolds number and the bulk-mean velocity in the uncontrolled case, i.e.

$$U_{b,NC}^+ = 5.1904 \log Re_b - 3.6741, \tag{2.5}$$

where the resultant bulk Reynolds number is calculated as $Re_b = 2U_b^+ Re_\tau$. Note that U_b can be calculated as

$$U_b = \frac{1}{2}\int_0^2 U(y)\,\mathrm{d}y, \tag{2.6}$$

where $U(y)$ is the streamwise velocity averaged in the streamwise and spanwise directions and time.

Figure 2 shows the drag-reduction rates at different y_d^+ values in all cases. Similarly to Hammond *et al.* (1998), we can obtain the maximum drag-reduction rate of $R_D \approx 25\,\%$ at $y_d^+ \approx 15$. Thus, the computational conditions in the present DNS can be considered sufficient for simulating a low-Reynolds-number turbulent channel flow.

3. Analytical methods

3.1. *Ordinal partition transition network*

Zhang *et al.* (2017*a*) proposed the multivariate OPTN considering the combination of permutation patterns extracted from n multivariate time series. Similarly to their study, we construct the multivariate OPTN to evaluate the correlations between temporal evolutions of the streamwise and wall-normal velocity fluctuations u' and v', respectively. Figure 3 shows the schematic of construction of the multivariate OPTN. First, we transform the elements of $\boldsymbol{u}$ $(= \{u'(t_i), u'(t_i + \tau_t), \ldots, u'(t_i + \tau_t(d_t - 1)\})$ and $\boldsymbol{v}$ $(= \{v'(t_i), v'(t_i + \tau_t), \ldots, v'(t_i + \tau_t(d_t - 1)\})$ into rank-order patterns (permutation patterns) based on the magnitude of these elements, where d_t is the embedding dimension (the rank-order pattern length) and τ_t is the delay time in a phase space (figure 3 represents the case of $d_t = 2$ and $\tau_t = \Delta t$). A combination of permutation patterns

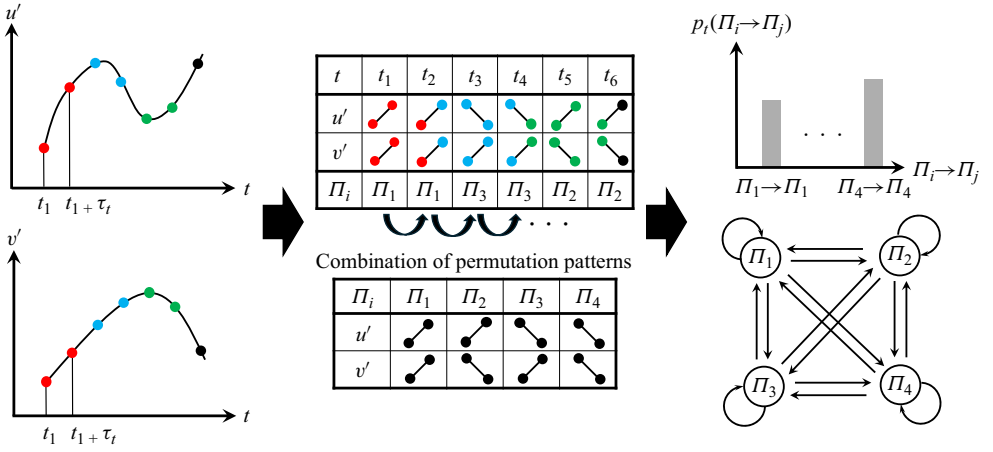

Figure 3. Schematic of construction of the multivariate OPTN when $d_t = 2$ and $\tau_t = \Delta t$.

$\Pi(= \{\Pi_1, \Pi_2, \ldots, \Pi_{d_t!^{2n}}\})$ corresponds to nodes in the network, and the link between two nodes is expressed by the transition probability from Π_i to Π_j, i.e. $p_t(\Pi_i \to \Pi_j)$. We calculate the multivariate OPTN entropy, i.e.

$$H_t = -\frac{\sum_{i=1}^{d_t!^n}\sum_{j=1}^{d_t!^n} p_t(\Pi_i \to \Pi_j)\ln p_t(\Pi_i \to \Pi_j)}{\ln (d_t!)^{2n}}, \tag{3.1}$$

where $0 \le H_t \le 1$. The multivariate OPTN entropy H_t can quantify the degree of randomness in the simultaneous dynamic behaviour of the two different time evolutions of u' and v'. We construct the multivariate OPTN from the temporal evolutions of u' and v' at the centre of each x–z plane, i.e. $x = L_x/2$, $0 \le y \le 1$ and $z = L_z/2$. The length of these time series is $t^+ \approx 10\,000$. To determine a suitable value of d_t, Nomi *et al.* (2021) proposed a method considering missing permutation patterns of a time series (Amigó, Zambrano & Sanjuán 2007). According to their study, missing permutation patterns appear at $d_t \ge 4$ for Gaussian noise. We also observe missing permutation patterns for fractional Brownian motion with the Hurst exponent of $1/3$ exhibiting Kolmogorov's five-third scaling law in the power spectrum (Meerschaert *et al.* 2014). These results mean that the values at $d_t \ge 4$ are not suitable for constructing the OPTN. Thus, we set $d_t = 3$. In this study, we define a local link strength between Π_i and Π_j as $s_{\Pi_i \to \Pi_j}(= p_t(\Pi_i \to \Pi_j))$. Note that $s_{\Pi_i \to \Pi_j}$ represents the transition degree between instantaneous fluid patterns.

To determine a suitable value of τ_t, we investigate the dependence of τ_t on H_t in the uncontrolled case. Figure 4 shows the variation in H_t as a function of y^+ at six different τ_t^+ values. In the cases of $\tau_t^+ = \Delta t^+$, $150\Delta t^+$ and $300\Delta t^+$, the dependence of H_t on y^+ is relatively small, whereas in the other cases, especially $\tau_t^+ = 30\Delta t^+$, H_t notably changes as a function of y^+. According to Mamori *et al.* (2023), the low-dimensional (high-dimensional) chaotic state of streamwise velocity fluctuations emerges at the viscous sublayer (logarithmic layer). This dynamical change from the low- to high-dimensional chaotic state increases the degree of randomness of streamwise velocity fluctuations with y^+. This trend can be clearly observed in the case of $\tau_t^+ = 30\Delta t^+ = 1.08$, which is the same as the value of τ_t mainly utilised by Mamori *et al.* (2023). Therefore, in this study, we

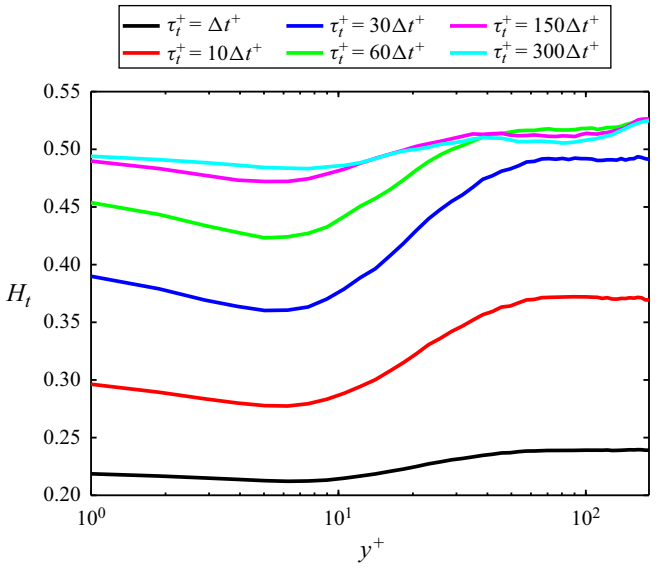

Figure 4. Variation in the multivariate OPTN entropy H_t as a function of y^+ at six different τ_t^+ values.

estimate the local link strength in the multivariate OPTN constructed at $\tau_t^+ = 30\Delta t^+ = 1.08$.

3.2. *Complexity–entropy causality plane*

The CECP (Zunino *et al.* 2012) considering a time-dependent approach, namely, the multiscale CECP, is useful for inferring the dynamical state in nonlinear systems. The CECP consists of the Jensen–Shannon complexity C_{JS} and PE H_p, i.e.

$$C_{JS}[\boldsymbol{P_p}] = Q_J[\boldsymbol{P_p}, \boldsymbol{P_e}]H_p[\boldsymbol{P_p}], \tag{3.2}$$

$$H_p[\boldsymbol{P_p}] = -\frac{\sum_{j=1}^{d_C!} p_p(\pi_j)\ln p_p(\pi_j)}{\ln d_C!}, \tag{3.3}$$

where Q_J is the disequilibrium, i.e.

$$Q_J[\boldsymbol{P_p}, \boldsymbol{P_e}] = \frac{H_p[(\boldsymbol{P_p}+\boldsymbol{P_e})/2] - H_p[\boldsymbol{P_p}]/2 - H_p[\boldsymbol{P_e}]/2}{Q_{J,max}}, \tag{3.4}$$

$$Q_{J,max} = -\frac{1}{2}\left\{\frac{d_C!+1}{d_C!}\ln(d_C!+1) - 2\ln(2d_C!) + \ln d_C!\right\}. \tag{3.5}$$

Here, $\boldsymbol{P_p} = \{p_p(\pi_j)\,|\,j = 1, 2, \ldots, d_C!)\}$ is the existing probability distribution of the permutation patterns π_j in the time series of u' and $\boldsymbol{P_e} = \{1/d_C!, 1/d_C!, \ldots, 1/d_C!\}$ is the uniform probability distribution, where d_C is the embedding dimension. Here, H_p represents the degree of randomness in the time evolution of u' and Q_J represents the disequilibrium in the probability distribution of the permutation patterns obtained from the time evolution of u'. In addition, C_{JS} is defined as the product of H_p and Q_J, which corresponds to the statistical complexity in the time evolution of u'.

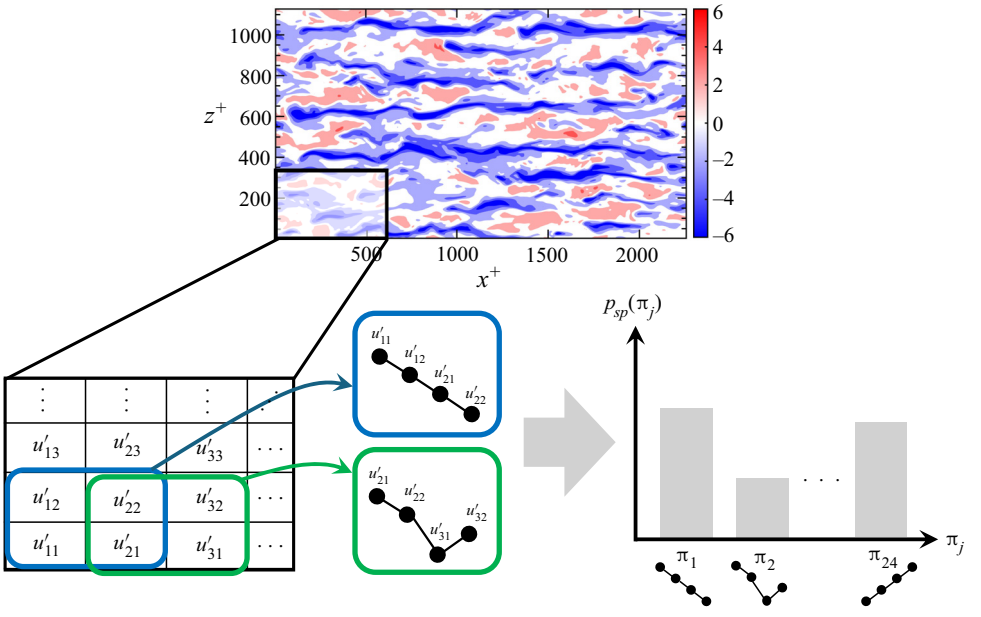

Figure 5. Schematic of transformation from u' to spatial permutation π_j when $d_x = d_z = 2$.

The dynamical state can be inferred from the shape of the trajectory on the CECP with the increasing delay time τ_C in d_C-dimensional phase space. If the dynamic behaviour exhibits deterministic chaos, a parabolic trajectory is drawn on the CECP. If the dynamic behaviour is strongly dominated by a stochastic process, no parabolic trajectory is drawn on the CECP and (H_p, C_{JS}) rapidly approaches $(1, 0)$ with increasing τ_C. Zunino *et al.* (2012) reported that τ_C at which C_{JS} takes a local maximum value corresponds to the minimal sampling rate required to capture all the information related to nonlinear correlations of the underlying chaotic dynamics. In this study, $d_C = 5$ and $0.036 \leq \tau_C^+ \leq 10.8$.

3.3. *Spatial permutation entropy*

The SPE (Zunino & Ribeiro 2016) enables us to quantitatively evaluate the degree of spatial randomness. Figure 5 shows a schematic of the transformation from u' to spatial permutation π_j. For the estimation of the SPE, we first construct permutation patterns in the extraction range of $d_x d_z$, i.e. motifs, where d_x and d_z represent the numbers of extracted points in the streamwise and spanwise directions, respectively (figure 5 represents the case of $d_x = d_z = 2$). Subsequently, all motifs in the entire spatial field are classified into each permutation pattern to generate the existing probability distribution $\boldsymbol{P_{sp}}$. We calculate the SPE H_{sp}, i.e.

$$H_{sp}[\boldsymbol{P_{sp}}] = -\frac{\sum_{j=1}^{(d_x d_z)!} p_{sp}(\pi_j) \ln p_{sp}(\pi_j)}{\ln (d_x d_z)!}, \tag{3.6}$$

where $0 \leq H_{sp} \leq 1$. Note that H_{sp} represents the degree of randomness in the instantaneous field of u'. Here, $\boldsymbol{P_{sp}} = \{p_{sp}(\pi_j) | j = 1, 2, \ldots, (d_x d_z)!\}$ is the existing

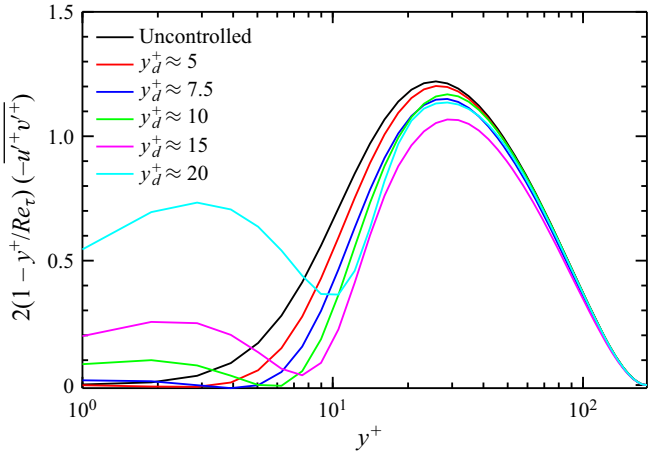

Figure 6. Weighted RSS in the uncontrolled and controlled cases.

probability distribution of the permutation patterns π_j in the spatial field data of u' in each x–z plane. In this study, $(d_x, d_z) = (3, 2)$.

4. Results and discussion

Figure 6 shows the weighted Reynolds shear stress (RSS) (Fukagata, Iwamoto & Kasagi 2002), i.e. $2(1 - y^+/Re_\tau)(-\overline{u'v'})$, in the uncontrolled and controlled cases. In the uncontrolled case, the weighted RSS is maximum at $y^+ \approx 25$, indicating that the suppression of the RSS in the region near the wall is of great importance for friction drag reduction. This result is very similar to that in the previous study by Fukagata *et al.* (2002). In the case of $y_d^+ \lesssim 10$, we observe the formation of the virtual wall in which the weighted RSS is approximately zero in the region between the wall and the detection plane, i.e. $0 \leqq y \leqq y_d$. On the other hand, in the case of $y_d^+ > 10$, the weighted RSS in the region near the wall markedly increases with y_d^+, leading to the smaller effect of the virtual wall. That is, the weighted RSS is not zero in the region of $0 \leqq y \leqq y_d$. Although the significant suppression of the weighted RSS results in the large drag-reduction effect in the case of $y_d^+ \approx 15$, the small drag-reduction effect in the case of $y_d^+ \approx 20$ is due to the smaller effect of the virtual wall. These results imply that the effect of the virtual wall markedly changes at $y_d^+ \approx 10$.

Figure 7 shows the variations in four different local link strengths $s_{\Pi_i \to \Pi_j}$ in the multivariate OPTN as a function of y^+ in the uncontrolled case. Note that Π_1, Π_6, Π_{31} and Π_{36} are dominant in the network, whereas the $s_{\Pi_i \to \Pi_j}$ of 32 other patterns have small values. We can observe a similar trend in all controlled cases (not shown here). Thus, we focus on these four patterns in this study. As shown in figure 7, they correspond to monotonically increasing and decreasing processes of both u' and v'. Furthermore, $s_{\Pi_6 \to \Pi_6}$ and $s_{\Pi_{31} \to \Pi_{31}}$, which are the local link strengths of the self-loop of nodes representing the negative correlation pattern between u' and v', are more dominant than $s_{\Pi_1 \to \Pi_1}$ and $s_{\Pi_{36} \to \Pi_{36}}$. Here, $s_{\Pi_6 \to \Pi_6}$ ($s_{\Pi_{31} \to \Pi_{31}}$) corresponds to the monotonically increasing (decreasing) process of u' and the decreasing (increasing) process of v'. The former local link strength represents the transition degree between instantaneous fluid patterns far from the wall being transported to the vicinity of the wall, whereas the latter local link strength represents that near the wall being transported away from the wall.

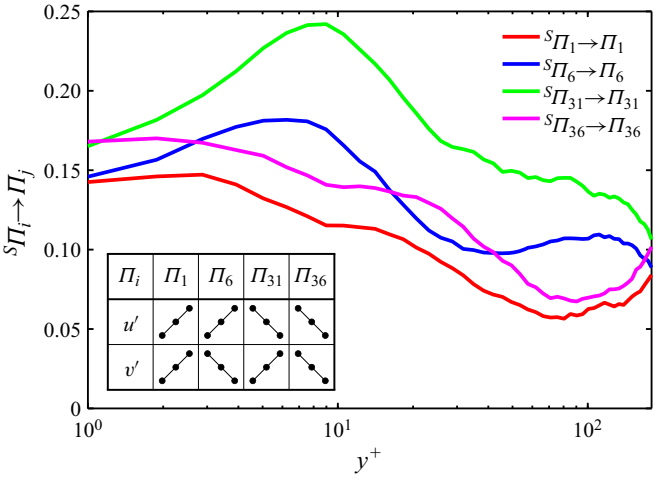

Figure 7. Four dominant local link strengths in the uncontrolled case.

In terms of the quadrant analysis proposed by Willmarth & Lu (1972),

$$\left.\begin{array}{l} \mathrm{Q1}: -u'v' < 0 \ (u' > 0,\ v' > 0), \\ \mathrm{Q2}: -u'v' > 0 \ (u' < 0,\ v' > 0), \\ \mathrm{Q3}: -u'v' < 0 \ (u' < 0,\ v' < 0), \\ \mathrm{Q4}: -u'v' > 0 \ (u' > 0,\ v' < 0), \end{array}\right\} \tag{4.1}$$

$s_{\Pi_6 \to \Pi_6}$ and $s_{\Pi_{31} \to \Pi_{31}}$ correspond to the Q4 and Q2 events, which denote the sweep and ejection generated by the streamwise vertical motions in the region near the wall, respectively. These events lead to a skin friction drag in turbulent flows. Namely, the regions where $s_{\Pi_6 \to \Pi_6}$ and $s_{\Pi_{31} \to \Pi_{31}}$ have large values are related to those where the ejection and sweep are induced. However, $s_{\Pi_6 \to \Pi_6}$ and $s_{\Pi_{31} \to \Pi_{31}}$ are maximum at $y^+ \approx 6$ and $y^+ \approx 9$, respectively, although, as shown in figure 6, the weighted RSS is maximum at $y^+ \approx 25$. In general, the amplitudes of u' and v' increase at $0 \leqq y^+ \lesssim 25$. Therefore, at $0 \leqq y^+ \lesssim 9$, not only the increases in the amplitudes of u' and v' but also the negative correlation between u' and v' results in the enhancement of the weighted RSS.

Figure 8 shows the variations in $s_{\Pi_i \to \Pi_j}$ as a function of y^+ in the uncontrolled and controlled cases. The solid and dashed lines denote the controlled and uncontrolled cases, respectively. The peak positions of $s_{\Pi_6 \to \Pi_6}$ and $s_{\Pi_{31} \to \Pi_{31}}$ shift away from the wall in all controlled cases. Similarly to the weighted RSS shown in figure 6, $s_{\Pi_6 \to \Pi_6}$ and $s_{\Pi_{31} \to \Pi_{31}}$ increase in the region near the wall owing to the opposition control. However, focusing on the region around the detection plane (black vertical line), $s_{\Pi_6 \to \Pi_6}$ and $s_{\Pi_{31} \to \Pi_{31}}$ decrease in the case of $y_d^+ < 10$ (figure 8*a*,*b*), whereas they increase in the case of $y_d^+ \gtrsim 10$ (figure 8*c*–*e*). In addition, the maximum $s_{\Pi_6 \to \Pi_6}$ and $s_{\Pi_{31} \to \Pi_{31}}$ in the case of $y_d^+ < 10$ remain almost unchanged, compared with those in the uncontrolled case. In the case of $y_d^+ \gtrsim 10$, they have larger values. On the other hand, the opposite trend of $s_{\Pi_1 \to \Pi_1}$ and $s_{\Pi_{36} \to \Pi_{36}}$ is observed in all controlled cases. According to these results, we can obtain the effect of the virtual wall by installing the detection plane closer to the wall than the position where $s_{\Pi_6 \to \Pi_6}$ and $s_{\Pi_{31} \to \Pi_{31}}$ in the uncontrolled case are maximum, i.e. $y_d^+ \lesssim 10$. In addition, in the cases where the virtual wall is clearly formed, $s_{\Pi_6 \to \Pi_6}$ and $s_{\Pi_{31} \to \Pi_{31}}$ are weaken around the detection plane owing to the effect of the virtual wall. Considering the relationship between the quadrant analysis and the local link strength

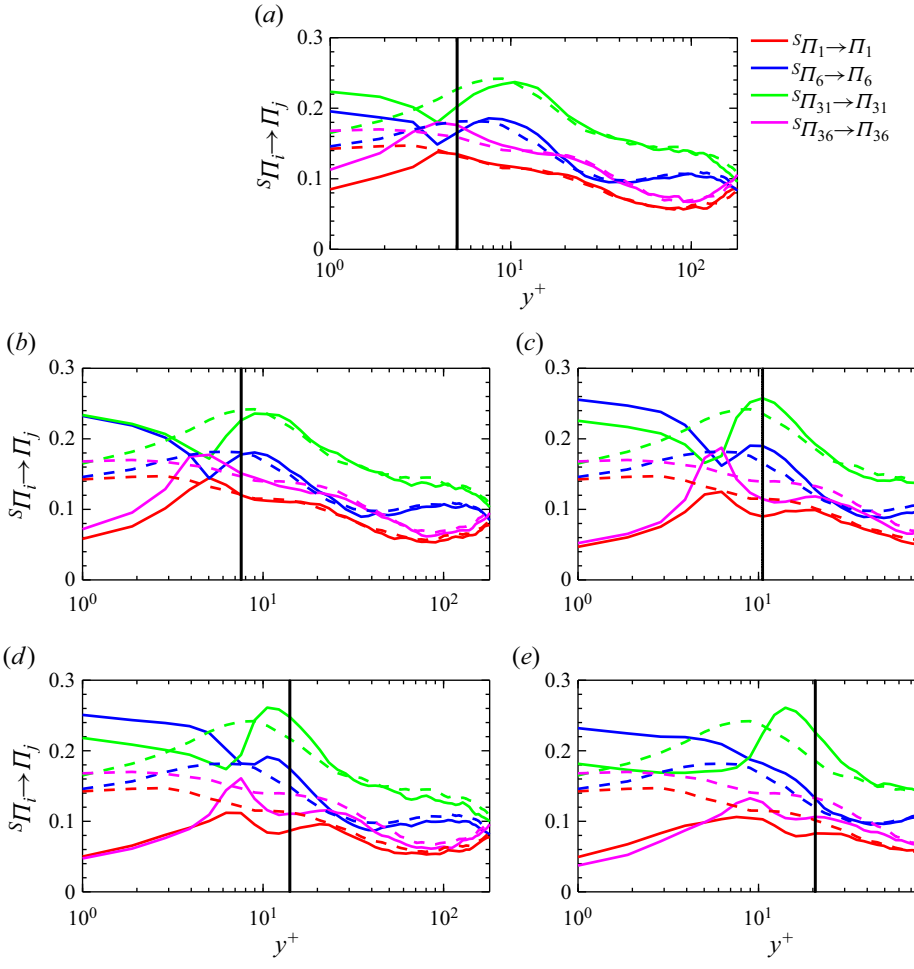

Figure 8. Four dominant local link strengths in five different controlled cases: (*a*) $y_d^+ \approx 5$; (*b*) $y_d^+ \approx 7.5$; (*c*) $y_d^+ \approx 10$; (*d*) $y_d^+ \approx 15$; (*e*) $y_d^+ \approx 20$. The black vertical line denotes the location of the detection plane. The solid and dashed lines denote the controlled and uncontrolled cases, respectively.

$s_{\Pi_i \to \Pi_j}$, the formation of the virtual wall weakens $s_{\Pi_6 \to \Pi_6}$ and $s_{\Pi_{31} \to \Pi_{31}}$ in the region around the detection plane, leading to the suppression of the ejection and sweep motions. These results suggest that the local link strength in the multivariate OPTN is useful for determining the location of the detection plane to maximise the effect of the virtual wall.

On the basis of the above-mentioned results, we focus on the spatiotemporal dynamics in the case of $y_d^+ \approx 10$ to investigate the effect of the virtual wall in more detail. Figures 9 and 10 show the trajectory and the right edge of the trajectory on the CECP at $y^+ \approx 5$, 20, 100 and 180 in the uncontrolled and controlled cases, respectively. As shown in figure 9, the trajectory exhibits a parabolic shape regardless of y^+ in the uncontrolled and controlled cases. In addition, the right edge of the trajectory shown in figure 10 approaches the bottom right corner of the CECP with increasing y^+, i.e. $(H_p, C_{JS}) = (1, 0)$. These indicate that the dynamical state of the streamwise velocity fluctuations represents chaos in the entire region of the channel. The randomness of u' increases with increasing y^+ in both the uncontrolled and controlled cases. These results in the

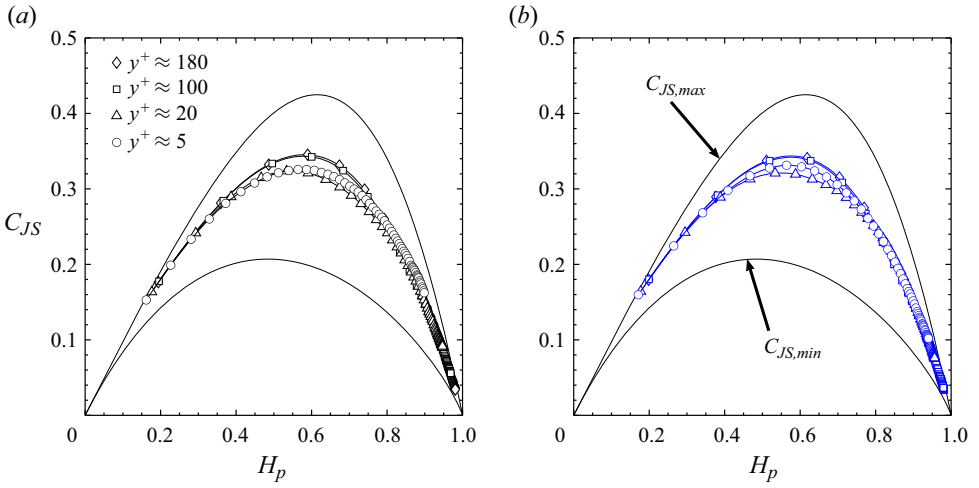

Figure 9. Trajectory on CECP in the uncontrolled and controlled cases at $y^+ \approx 5$, 20 and 100: (*a*) uncontrolled case; (*b*) controlled case; ◯, $y^+ \approx 5$; △, $y^+ \approx 20$; □, $y^+ \approx 100$; ◇, $y^+ \approx 180$.

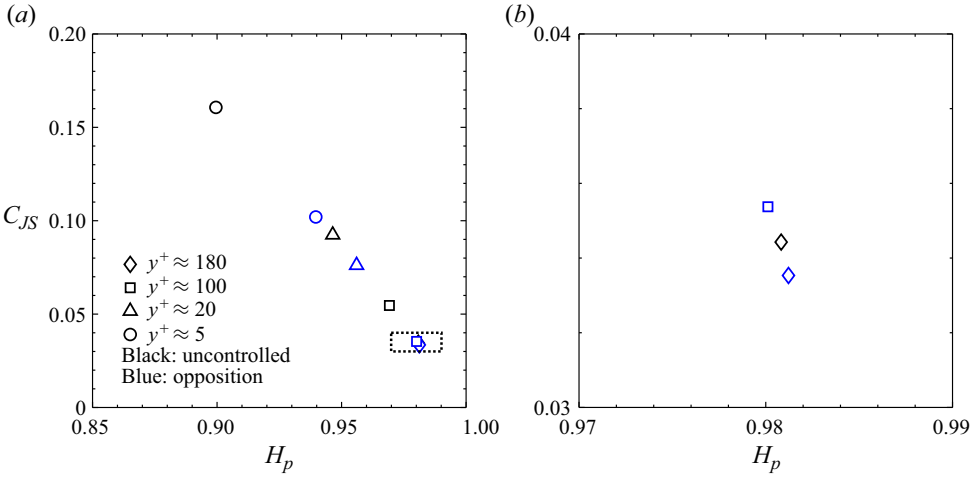

Figure 10. Right edge of the trajectory on CECP in the uncontrolled and controlled cases at $y^+ \approx 5$, 20, 100 and 180: (*a*) overview; (*b*) enlarged view of the black dotted rectangular region in (*a*); black, uncontrolled; blue, opposition ($y_d^+ \approx 10$); ◯, $y^+ \approx 5$; △, $y^+ \approx 20$; □, $y^+ \approx 100$; ◇, $y^+ \approx 180$.

uncontrolled case sufficiently support the findings obtained by the orbital-instability-based forecasting method and the univariate OPTN in combination with surrogate data methods (Mamori *et al.* 2023). According to previous studies (Smith & Metzler 1983; Bae & Lee 2021), streaks actively coalesce and separate in the buffer layer, whereas the coalescence of several short streaks forms large-scale streaks with long lifetimes in the viscous sublayer. The presence of large-scale streaks leads to the low-dimensional chaotic state of u' in the viscous sublayer, whereas the active coalescence and separation of streaks significantly produce a higher randomness of u' in the buffer layer. In the controlled case (figures 9*b* and 10), the right edge of the trajectory on the CECP approaches the bottom right corner of the CECP, compared with the uncontrolled case, indicating that the dynamic behaviour of the controlled u' exhibits a higher randomness. As shown in

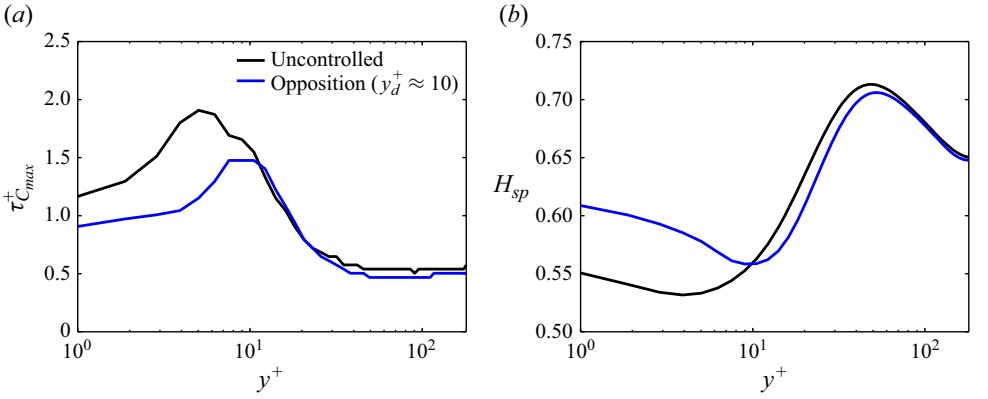

Figure 11. Variations in $\tau^+_{C_{max}}$ and H_{sp} as a function of y^+: (*a*) $\tau^+_{C_{max}}$; (*b*) H_{sp}; black, uncontrolled; blue, opposition ($y_d^+ \approx 10$).

figure 6, the opposition control increases the weighted RSS in the region near the wall, leading to the enhancement of turbulent motions. In the buffer and logarithmic layers, the characteristics of the drag-reducing flow field under the CPG condition (Hasegawa, Quadrio & Frohnapfel 2014; Nabae *et al.* 2020) produce the high-dimensional chaotic state of u'. According to Hasegawa *et al.* (2014), although an adequate flow control significantly decreases the friction drag in the region near the wall, the increase in energy flux in the drag-reducing flow does not result in an essential change in flow field under the CPG condition. Therefore, the dynamical state of u' in the controlled case represents chaos with high randomness in the entire region of the channel. This has not been revealed in the previous studies on the dynamic behaviour of a turbulent channel flow.

Figure 11 shows the variations in $\tau^+_{C_{max}}$ and H_{sp} as functions of y^+ in the uncontrolled and controlled cases. Here, $\tau^+_{C_{max}}$ represents the delay time at which C_{JS} takes a local maximum value. In the uncontrolled case, $\tau^+_{C_{max}}$ (H_{sp}) rapidly decreases (increases) in the buffer layer, indicating the rapid increase in the complexity of u' in the buffer layer. As in figure 9, this is due to the active coalescence and separation of streaks. Smith & Metzler (1983) reported that the active coalescence and separation of streaks in the buffer layer result in the rapid increases in the mean and variance of the spanwise spacing of streaks. This region approximately corresponds to the region where $\tau^+_{C_{max}}$ (H_{sp}) rapidly decreases (increases). As shown in figure 11, the opposition control allows the region where $\tau^+_{C_{max}}$ (H_{sp}) rapidly decreases (increases) to be reduced significantly. This indicates that the control reduces the region where streaks actively coalesce and separate. In addition, H_{sp} decreases at $y^+ \gtrsim 10$ compared with the uncontrolled case, suggesting that the coalescence and separation of streaks are suppressed.

Figure 12 shows the instantaneous u', i.e. streak structures, at $y^+ \approx 1$, 6 and 15 in the uncontrolled and controlled cases. Note that the black line represents the threshold of u' to identify the cluster, i.e. $u' = -\alpha u'_{rms,NC}$ (see Appendix A for details). As shown in figure 12(*a*,*b*), in the quite-near-wall region ($y^+ \approx 1$), small-scale structures are dominant in the controlled case. In the region around the virtual wall, i.e. $y^+ \approx 6$ (figure 12*c*,*d*), although the streak structures are suppressed significantly, the small-scale structures are relatively dominant in the controlled case. These small-scale structures make the flow field in the controlled case more complex than that in the uncontrolled case, leading to the increase in H_{sp} in the viscous sublayer ($y^+ < 10$). On the other hand, figure 12(*e*,*f*) shows

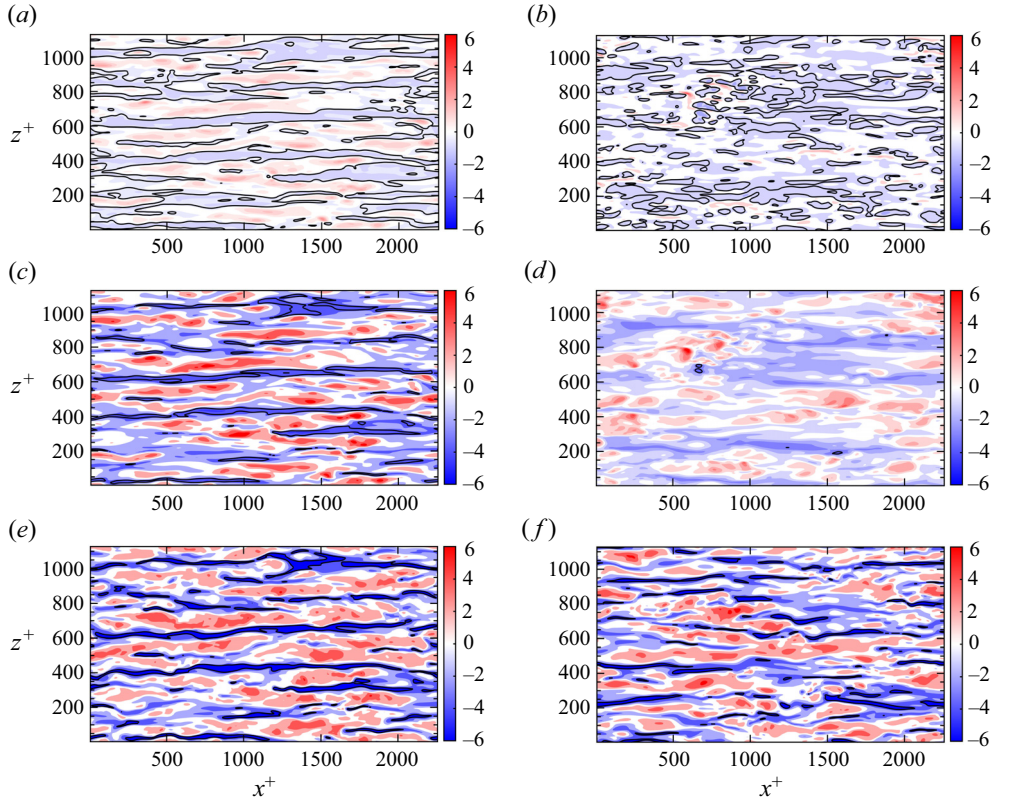

Figure 12. Visualisation of instantaneous streamwise velocity fluctuations u' (streak structures): (a,b) $y^+ \approx 1$; (c,d) $y^+ \approx 6$; (e,f) $y^+ \approx 15$; (a,c,e) uncontrolled; (b,d,f) opposition ($y_d^+ \approx 10$). Colors represents the values of u'.

that the control slightly suppresses the streak structures and decreases the large-scale structures in the streamwise direction. The suppression of the streak structures leads to the slight decrease in the large-scale structures generated by the coalescence of streaks. Subsequently, the small-scale structures generated by the separation of streaks decrease, leading to the decrease in H_{sp} in the buffer layer ($y^+ \gtrsim 10$).

To identify the relationship of the variations in $\tau^+_{C_{max}}$ and H_{sp} with the streak structures in more detail, we investigate the meandering behaviour of streaks in uncontrolled and controlled cases. Note that the detailed methods for quantifying the meandering magnitude and streamwise length of streaks are described in Appendix A. Figure 13 shows the mean meandering magnitudes $\overline{\xi^+_{rms}}$ and streamwise length $\overline{l^+_x}$ of individual u' structures, together with their standard deviations, $\sigma_{\xi^+_{rms}}$ and $\sigma_{l^+_x}$, respectively. In the uncontrolled case, all these values are small in the viscous sublayer, whereas they rapidly increase in the buffer layer. That is, the meandering magnitude and streamwise length of streaks are small (large) in the viscous sublayer (buffer layer). In addition, we observe a wide variety of meandering magnitudes and streamwise lengths of streaks with increasing y^+. The active coalescence and separation of streaks in the buffer layer (Smith & Metzler 1983) increase the variety of streamwise lengths of streaks, and the meandering magnitude of streaks depends on their streamwise length (Bae & Lee 2021; Hwang & Lee 2022). They are strongly associated with the formation of a wide variety of meandering magnitudes and streamwise lengths of streaks. In the controlled case, all the values shown in figure 13 decrease in the

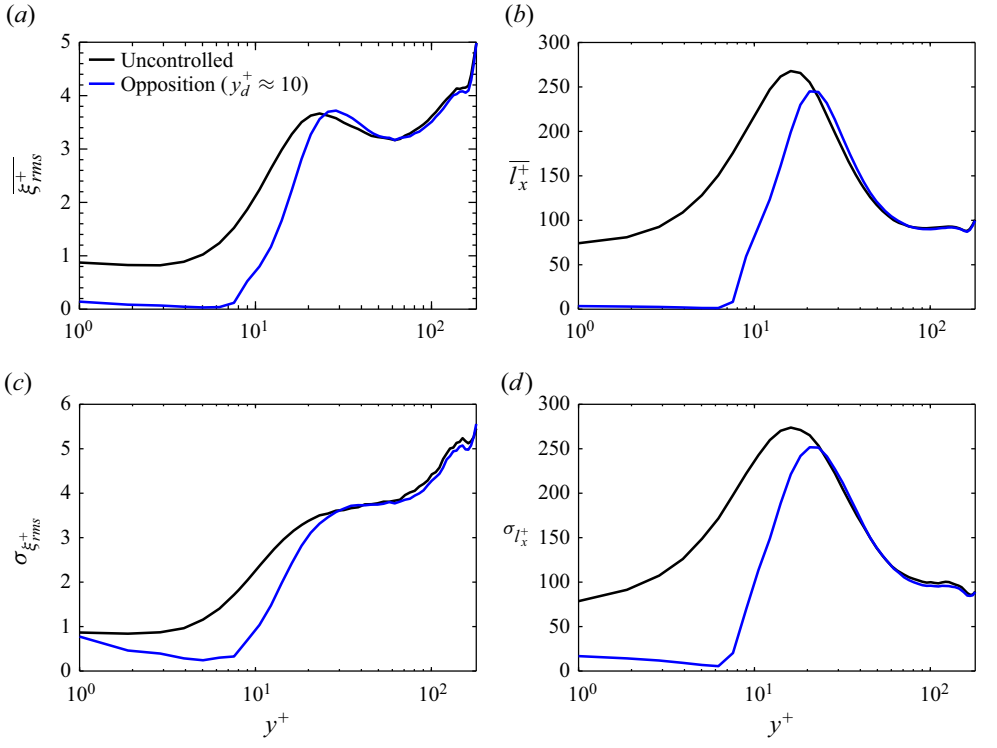

Figure 13. (*a*) Mean meandering magnitude $\overline{\xi_{rms}^+}$; (*b*) mean streamwise length $\overline{l_x^+}$; (*c*) standard deviation of meandering magnitude $\sigma_{\xi_{rms}^+}$; (*d*) standard deviation of streamwise length $\sigma_{l_x^+}$; black, uncontrolled; blue, opposition ($y_d^+ \approx 10$).

viscous sublayer and buffer layer (especially, in the region below the detection plane, i.e. $y^+ \leq 10$), indicating that the control decreases the variety of meandering magnitudes and streamwise lengths of streaks. This means that the coalescence and separation of streaks are suppressed. The results shown in figures 12 and 13 strongly support the physical mechanism identified by the multiscale CECP and SPE (figure 11).

We here investigate the turbulent energy transport to obtain deeper insights into the drag-reduction mechanism. Figure 14 shows the streamwise components of the production $P_{u'u'}$ and dissipation $\epsilon_{u'u'}$ and the three components of the pressure strain term Π_i^s. In the viscous sublayer, the enhancement of turbulence by the opposition control leads to the increase in $P_{u'u'}$. In addition, the control eliminates the contribution from the viscous diffusion, leading to a significant decrease in the absolute value of $\epsilon_{u'u'}$. In the buffer layer, compared with the uncontrolled case, $P_{u'u'}$ decreases significantly, whereas the absolute value of $\epsilon_{u'u'}$ hardly decreases. This means that the dissipation rate for the generated turbulent energy increases compared with the uncontrolled case. As can be observed in figure 14(*b*), the absolute values of the pressure strain in the wall-normal and spanwise directions (Π_2^s and Π_3^s, respectively) decrease in the viscous sublayer and buffer layer, whereas that in the streamwise direction (Π_1^s) increases (decreases) in the viscous sublayer (buffer layer). The trend of Π_1^s is similar to that of $P_{u'u'}$. In addition, the decreases in the absolute values of Π_2^s and Π_3^s indicate that the pressure redistribution of turbulent energy from u' to v' and w' is suppressed, which is related to the regeneration cycle in turbulent flows (Hamilton, Kim & Waleffe 1995). Since the wavy motions of streaks (i.e. the streak meandering) plays an important role in this pressure redistribution of turbulent energy

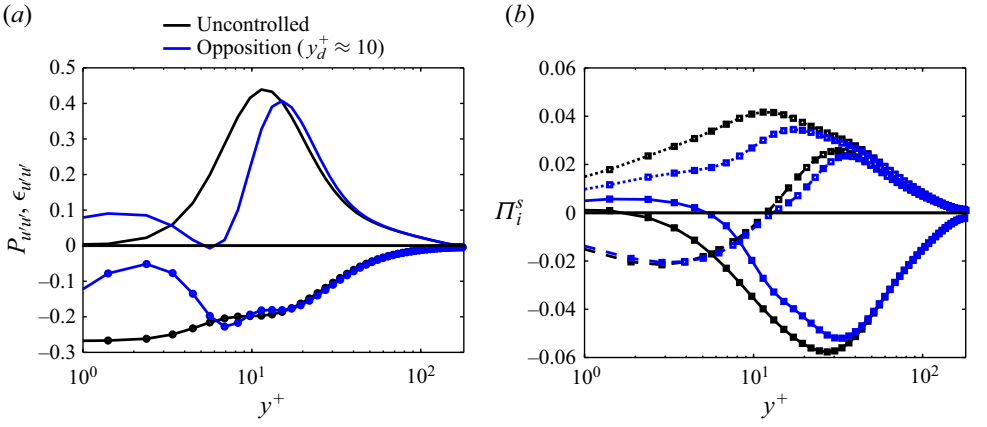

Figure 14. (*a*) Streamwise components of production and dissipation terms; (*b*) pressure strain term; no marker, production; ◯, dissipation; □, pressure strain; solid line, streamwise component; dashed line, wall-normal component; dotted line, spanwise component; black, uncontrolled; blue, opposition ($y_d^+ \approx 10$).

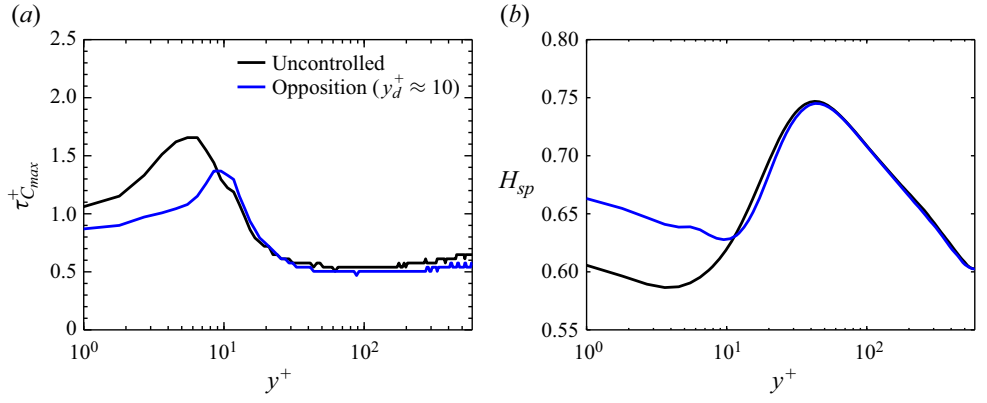

Figure 15. Variations in $\tau^+_{C_{max}}$ and H_{sp} as functions of y^+ at a high Reynolds number of $Re_\tau = 590$: (*a*) $\tau^+_{C_{max}}$; (*b*) H_{sp}; black, uncontrolled; blue, opposition ($y_d^+ \approx 10$).

(Kawata & Tsukahara 2021), this is due to the suppression of streak meandering motions shown in figure 13. That is, the opposition control suppresses the regeneration cycle in the region near the wall. This region corresponds reasonably well to the region with actively coalesced and separated streaks that is identified by the multiscale CECP and SPE.

Finally, we investigate the Reynolds number effect on the drag-reduction mechanism proposed in this study. Figure 15 shows the variations in $\tau^+_{C_{max}}$ and H_{sp} as functions of y^+ in the uncontrolled and controlled cases at a higher Reynolds number of $Re_\tau = 590$. Similarly to figure 11, the detection plane is set to $y_d^+ \approx 10$. The trends shown in figure 15 are very similar to those observed in figure 11. That is, the Reynolds number dependence of the drag-reduction mechanism is relatively small, suggesting that the drag-reduction mechanism proposed in this study is applicable to a wide range of Reynolds numbers.

In this study, we have focused mainly on the applicability of the ordinal pattern-based analysis to revealing the drag-reduction mechanism of an opposition-controlled turbulent channel flow. The detection plane has been determined by a phenomenalistic approach based on visualised flow structures (Hammond *et al.* 1998; Chung & Talha 2011).

Other recent studies on opposition control (Stroh *et al.* 2015; Wang *et al.* 2022; Dacome *et al.* 2024) have not provided a methodology to optimise the detection plane. The local link strength in the multivariate OPTN we adopted in this study is an applicable network metric for determining the detection location for opposition control. The drag-reduction effect is significantly associated with the reduction of the region where streaks actively coalesce and separate and the suppression of the regeneration cycle in the region near the wall. To the best of the authors' knowledge, this is the first study to provide (i) an indicator for appropriately determining the location of the detection plane and (ii) a new interpretation of the drag-reduction mechanism derived from the ordinal pattern-based analysis. In our future work, we will apply the ordinal pattern-based analysis to other control methods and attempt to propose new control strategies.

5. Summary

We have conducted a numerical study on the drag-reduction mechanism of an opposition-controlled turbulent channel flow under a low-Reynolds-number condition from the viewpoint of the symbolic dynamics approach. In this study, we have applied the ordinal pattern-based analysis considering the multivariate OPTN, multiscale CECP and SPE to the flow field with and without the opposition control. The local link strength of the self-loop of nodes representing the negative correlation pattern between u' and v' is predominant in the multivariate OPTN in both the uncontrolled and controlled cases. The effect of the virtual wall generated by the opposition control is maximum at $y_d^+ \approx 10$. This location of the detection plane corresponds to the wall-normal location where the local link strength is maximised in the uncontrolled case. These results suggest that the local link strength in the multivariate OPTN has potential use in appropriately determining the location of the detection plane to control a turbulent channel flow. The drag reduction by the opposition control is mainly attributed to the reduction of the region where streaks actively coalesce and separate and the suppression of the regeneration cycle in the region near the wall. This is reasonably identified by the multiscale CECP and SPE.

Acknowledgement. Y.N. is grateful to Dr. H. Mamori (The University of Electro-Communications) for fruitful discussions.

Funding. This study was partially supported by the Ebara Hatakeyama memorial foundation.

Declaration of interests. The authors report no conflict of interest.

Data availability. The data that support the findings of this study are available from the corresponding author upon reasonable request.

Author ORCIDs.
Hiroshi Gotoda https://orcid.org/0000-0001-6402-8510;
Yusuke Nabae https://orcid.org/0000-0001-7560-5053.

Appendix A. Methods for quantifying meandering magnitude and streamwise length of streaks

We apply the cluster detection and conditional sampling techniques to the instantaneous u' to quantify the meandering magnitude and streamwise length of streaks. Similarly to Hwang & Sung (2018) and Hwang & Lee (2022), we define the clusters of negative u' as

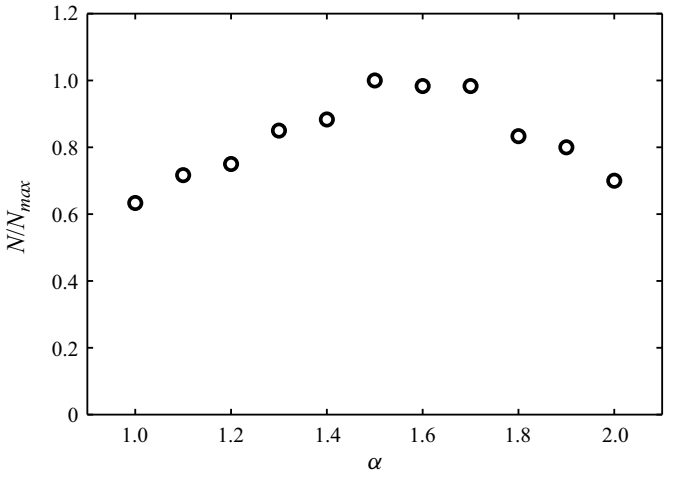

Figure 16. Ratio of the total number of clusters at each α to the maximum N (N/N_{max}) identified by percolation analysis (Moisy & Jiménez 2004; del Álamo *et al.* 2006; Lozano-Durán *et al.* 2012).

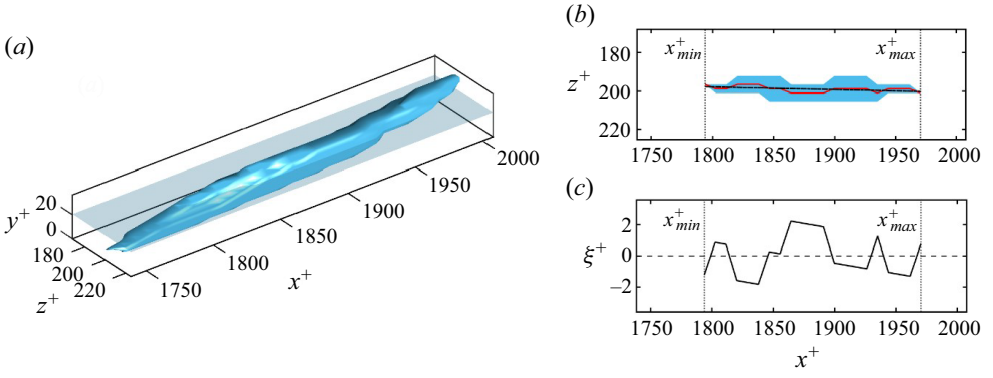

Figure 17. Visualisation of a cluster extracted from an instantaneous flow field: (*a*) three-dimensional view; (*b*) two-dimensional view at $y^+ \approx 20$; (*c*) variation in the spine of the streak ($\xi^+ = z^+_{spine} - z^+_{fit}$) at $y^+ \approx 20$. In (*b*) and (*c*), the red solid line represents the spine of the light blue region (z^+_{spine}) and the black dash-dotted line represents the linear fit of the spine (z^+_{fit}).

the group of connected points satisfying

$$u' < -\alpha u'_{rms,NC}, \tag{A1}$$

where $u'_{rms,NC}$ is the root mean square (RMS) of u' in the uncontrolled case and α is the threshold. The threshold α can be determined by the percolation analysis (Moisy & Jiménez 2004; del Álamo *et al.* 2006; Lozano-Durán, Flores & Jiménez 2012) of the uncontrolled flow field. Figure 16 shows the ratio of the total number of clusters at each α to the maximum N (N/N_{max}) identified by percolation analysis, where N and N_{max} represent the total number of clusters at each α and the maximum N over α, respectively. The number of clusters is maximised at $\alpha = 1.5$. Thus, we set $\alpha = 1.5$.

Subsequently, from the cluster shape identified by (A1), we quantify the meandering magnitude and streamwise length of streaks in each x–z plane. Figure 17(*a*,*b*) shows a three-dimensional view of a cluster extracted from an instantaneous u' and a two-dimensional view at $y^+ \approx 20$ in (*a*), respectively. The light blue region in figure 17(*b*)

represents the region identified as the cluster at the corresponding y^+. The spine location z^+_{spine} (red solid line) is defined as the mean spanwise location of the light blue region at each streamwise location, i.e.

$$z^+_{spine} = \tfrac{1}{2}(z^+_{max} + z^+_{min}), \tag{A2}$$

where z^+_{max} and z^+_{min} represent the maximum and minimum spanwise locations of the light blue region at each streamwise location, respectively. Then, we obtain the linear fit z^+_{fit} (black dash-dotted line) from z^+_{spine}. The meandering of z^+_{spine} (ξ^+) is defined as the difference in spanwise location between z^+_{spine} and z^+_{fit}, i.e.

$$\xi^+ = z^+_{spine} - z^+_{fit}. \tag{A3}$$

On the basis of the variation in ξ^+ as a function of x^+ (figure 17*c*), we can quantify the meandering magnitude by measuring the RMS of ξ^+ (i.e. ξ^+_{rms}). In addition, the difference between the maximum and minimum streamwise locations in the light blue region, x^+_{max} and x^+_{min}, respectively, is defined as the streamwise length l^+_x of streaks, i.e.

$$l^+_x = x^+_{max} - x^+_{min}. \tag{A4}$$

References

del Álamo, J.C., Jiménez, J., Zandonade, P. & Moser, R.D. 2006 Self-similar vortex clusters in the turbulent logarithmic region. *J. Fluid Mech.* **561**, 329–358.

Amigó, J.M. 2010 *Permutation Complexity in Dynamical Systems: Ordinal Patterns, Permutation Entropy and All That*. Springer Science & Business Media.

Amigó, J.M., Zambrano, S. & Sanjuán, M.A.F. 2007 True and false forbidden patterns in deterministic and random dynamics. *Europhys. Lett.* **79** (5), 50001.

Aubry, N., Holmes, P., Lumley, J.L. & Stone, E. 1988 The dynamics of coherent structures in the wall region of a turbulent boundary layer. *J. Fluid Mech.* **192**, 115–173.

Bae, H.J. & Lee, M. 2021 Life cycle of streaks in the buffer layer of wall-bounded turbulence. *Phys. Rev. Fluids* **6**, 064603.

Bandt, C. & Pompe, B. 2002 Permutation entropy: a natural complexity measure for time series. *Phys. Rev. Lett.* **88**, 174102.

Caballero-Pintado, V., Matilla-Garcia, M. & Marin, M.R. 2018 Symbolic recurrence plots to analyze dynamical systems. *Chaos* **28**, 063112.

Cavalieri, A.V.G. 2021 Structure interactions in a reduced-order model for wall-bounded turbulence. *Phys. Rev. Fluids* **6** (3), 034610.

Cavalieri, A.V.G. & Nogueira, P.A.S. 2022 Reduced-order Galerkin models of plane Couette flow. *Phys. Rev. Fluids* **7** (10), L102601.

Cavalieri, A.V.G., Rempel, E.L. & Nogueira, P.A.S. 2022 Transition to chaos in a reduced-order model of a shear layer. *J. Fluid Mech.* **932**, A43.

Choi, H., Moin, P. & Kim, J. 1994 Active turbulence control for drag reduction in wall-bounded flows. *J. Fluid Mech.* **262**, 75–110.

Chowdhuri, S., Iacobello, G. & Banerjee, T. 2021 Visibility network analysis of large-scale intermittency in convective surface layer turbulence. *J. Fluid Mech.* **925**, A38.

Chung, Y.M. & Talha, T. 2011 Effectiveness of active flow control for turbulent skin friction drag reduction. *Phys. Fluids* **23** (2), 025102.

Dacome, G., Mörsch, R., Kotsonis, M. & Baars, W.J. 2024 Opposition flow control for reducing skin-friction drag of a turbulent boundary layer. *Phys. Rev. Fluids* **9** (6), 064602.

De, S., Gupta, S., Unni, V.R., Ravindran, R., Kasthuri, P., Marwan, N., Kurths, J. & Sujith, R.I. 2023 Study of interaction and complete merging of binary cyclones using complex networks. *Chaos* **33**, 013129.

Dukowicz, J.K. & Dvinsky, A.S. 1992 Approximate factorization as a high order splitting for the implicit incompressible flow equations. *J. Comput. Phys.* **102**, 336–347.

Eckhardt, B. & Mersmann, A. 1999 Transition to turbulence in a shear flow. *Phys. Rev.* E **60** (1), 509.

FUKAGATA, K., IWAMOTO, K. & HASEGAWA, Y. 2024 Turbulent drag reduction by streamwise traveling waves of wall-normal forcing. *Annu. Rev. Fluid Mech.* **56**, 69–90.
FUKAGATA, K., IWAMOTO, K. & KASAGI, N. 2002 Contribution of Reynolds stress distribution to the skin friction in wall-bounded flows. *Phys. Fluids* **14**, L73–L76.
FUKAGATA, K., KASAGI, N. & KOUMOUTSAKOS, P. 2006 A theoretical prediction of friction drag reduction in turbulent flow by superhydrophobic surfaces. *Phys. Fluids* **18**, 051703.
GAO, Z. & JIN, N. 2009 Flow-pattern identification and nonlinear dynamics of gas-liquid two-phase flow in complex networks. *Phys. Rev.* E **79**, 066303.
GOTODA, H., KOBAYASHI, H. & HAYASHI, K. 2017*a* Chaotic dynamics of a swirling flame front instability generated by a change in gravitational orientation. *Phys. Rev.* E **95**, 022201.
GOTODA, H., PRADAS, M. & KALLIADASIS, S. 2017*b* Chaotic versus stochastic behavior in active-dissipative nonlinear systems. *Phys. Rev. Fluids* **2**, 124401.
HAMILTON, J.M., KIM, J. & WALEFFE, F. 1995 Regeneration mechanisms of near-wall turbulence structures. *J. Fluid Mech.* **287**, 317–348.
HAMMOND, E.P., BEWLEY, T.R. & MOIN, P. 1998 Observed mechanisms for turbulence attenuation and enhancement in opposition-controlled wall-bounded flows. *Phys. Fluids* **10**, 2421–2423.
HASEGAWA, Y., QUADRIO, M. & FROHNAPFEL, B. 2014 Numerical simulation of turbulent duct flows with constant power input. *J. Fluid Mech.* **750**, 191–209.
HAYASHI, K., GOTODA, H. & GENTILI, P.L. 2016 Probing and exploiting the chaotic dynamics of a hydrodynamic photochemical oscillator to implement all the basic binary logic functions. *Chaos* **26**, 053102.
HOLMES, P., LUMLEY, J.L. & BERKOOZ, G. 1996 *Turbulence, Coherent Structures, Dynamical Systems and Symmetry*, Cambridge Monographs on Mechanics. Cambridge University Press.
HWANG, J. & LEE, J.H. 2022 Meandering features of wall-attached structures in turbulent boundary layer. *Phys. Rev. Fluids* **7**, 114603.
HWANG, J. & SUNG, H.J. 2018 Wall-attached structures of velocity fluctuations in a turbulent boundary layer. *J. Fluid Mech.* **856**, 958–983.
IACOBELLO, G., RIDOLFI, L. & SCARSOGLIO, S. 2021 Large-to-small scale frequency modulation analysis in wall-bounded turbulence via visibility networks. *J. Fluid Mech.* **918**, A13.
IACOBELLO, G., SCARSOGLIO, S., KUERTEN, J.G.M. & RIDOLFI, L. 2018 Spatial characterization of turbulent channel flow via complex networks. *Phys. Rev.* E **98**, 013107.
KASAGI, N., SUZUKI, Y. & FUKAGATA, K. 2009 Microelectromechanical systems–based feedback control of turbulence for skin friction reduction. *Annu. Rev. Fluid Mech.* **41**, 231–251.
KAWATA, T. & TSUKAHARA, T. 2021 Scale interactions in turbulent plane Couette flows in minimal domains. *J. Fluid Mech.* **911**, A55.
KIM, J. 2003 Control of turbulent boundary layers. *Phys. Fluids* **15**, 1093–1105.
KOBAYASHI, W., GOTODA, H., KANDANI, S., OHMICHI, Y. & MATSUYAMA, S. 2019 Spatiotemporal dynamics of turbulent coaxial jet analyzed by symbolic information-theory quantifiers and complex-network approach. *Chaos* **29**, 123110.
KULP, C.W. & ZUNINO, L. 2014 Discriminating chaotic and stochastic dynamics through the permutation spectrum test. *Chaos* **24**, 033116.
LACASA, L., LUQUE, B., BALLESTEROS, F., LUQUE, J. & NUNO, J.C. 2008 From time series to complex networks: the visibility graph. *Proc. Natl Acad. Sci.* **105**, 4972–4975.
LI, Q. & ZUNTAO, F. 2014 Permutation entropy and statistical complexity quantifier of nonstationarity effect in the vertical velocity records. *Phys. Rev.* E **89**, 012905.
LOZANO-DURÁN, A., FLORES, O. & JIMÉNEZ, J. 2012 The three-dimensional structure of momentum transfer in turbulent channels. *J. Fluid Mech.* **694**, 100–130.
LOZANO-DURÁN, A., JIMÉNEZ, J. 2014 Time-resolved evolution of coherent structures in turbulent channels: characterization of eddies and cascades. *J. Fluid Mech.* **759**, 432–471.
MAMORI, H., NABAE, Y., FUKUDA, S. & GOTODA, H. 2023 Dynamic state of low-Reynolds-number turbulent channel flow. *Phys. Rev.* E **108**, 025105.
MARWAN, N., ROMANO, M.C., THIEL, M. & KURTHS, J. 2007 Recurrence plots for the analysis of complex systems. *Phys. Rep.* **438**, 237–329.
MCCULLOUGH, M., SAKELLARIOU, K., STEMLER, T. & SMALL, M. 2016 Counting forbidden patterns in irregularly sampled time series. I. The effects of under-sampling, random depletion, and timing jitter. *Chaos* **26**, 123103.
MCCULLOUGH, M., SMALL, M., STEMLER, T. & IU, H.H.-C. 2015 Time lagged ordinal partition networks for capturing dynamics of continuous dynamical systems. *Chaos* **25**, 053101.

MEERSCHAERT, M.M., SABZIKAR, F., PHANIKUMAR, M.S. & ZELEKE, A. 2014 Tempered fractional time series model for turbulence in geophysical flows. *J. Stat. Mech.: Theory Exp.* P09023.

MOEHLIS, J., FAISST, H. & ECKHARDT, B. 2004 A low-dimensional model for turbulent shear flows. *New J. Phys.* **6** (1), 56.

MOISY, F. & JIMÉNEZ, J. 2004 Geometry and clustering of intense structures in isotropic turbulence. *J. Fluid Mech.* **513**, 111.

MORINISHI, Y., LUND, T.S., VASILYEV, O.V. & MOIN, P. 1998 Fully conservative higher order finite difference schemes for incompressible flow. *J. Comput. Phys.* **143**, 90–124.

MURAYAMA, S., KINUGAWA, H., TOKUDA, I.T. & GOTODA, H. 2018 Characterization and detection of thermoacoustic combustion oscillations based on statistical complexity and complex-network theory. *Phys. Rev.* E **97**, 022223.

NABAE, Y. & FUKAGATA, K. 2024 Theoretical and numerical analyses of turbulent plane Couette flow controlled using uniform blowing and suction. *Intl J. Heat Fluid Flow* **106**, 109286.

NABAE, Y., KAWAI, K. & FUKAGATA, K. 2020 Prediction of drag reduction effect by streamwise traveling wave-like wall deformation in turbulent channel flow at practically high Reynolds numbers. *Intl J. Heat Fluid Flow* **82**, 108550.

NOMI, Y., GOTODA, H., KANDANI, S. & ALMARCHA, C. 2021 Complex network analysis of the gravity effect on premixed flames propagating in a Hele-Shaw cell. *Phys. Rev.* E **103**, 022218.

RICCO, P., SKOTE, M. & LESCHZINER, M.A. 2021 A review of turbulent skin-friction drag reduction by near-wall transverse forcing. *Prog. Aerosp. Sci.* **123**, 100713.

ROSSO, O.A., LARRONDO, H.A., MARTIN, M.T., PLASTINO, A. & M.A. FUENTES 2007 Distinguishing noise from chaos. *Phys. Rev. Lett.* **99**, 154102.

SANGHI, S. & AUBRY, N. 1993 Mode interaction models for near-wall turbulence. *J. Fluid Mech.* **247**, 455–488.

SMALL, M. 2013 Complex networks from time series: capturing dynamics. *Proceedings of the 2013 IEEE International Symposium on Circuits and Systems*, pp. 2509–2512.

SMITH, C.R. & METZLER, S.P. 1983 The characteristics of low-speed streaks in the near-wall region of a turbulent boundary layer. *J. Fluid Mech.* **129**, 27–54.

SPALART, P.R., MOSER, R.D. & ROGERS, M.M. 1991 Spectral methods for the Navier–Stokes equations with one infinite and two periodic directions. *J. Comput. Phys.* **96**, 297–324.

STROH, A., FROHNAPFEL, B., SCHLATTER, P. & HASEGAWA, Y. 2015 A comparison of opposition control in turbulent boundary layer and turbulent channel flow. *Phys. Fluids* **27** (7), 075101.

TAIRA, K., NAIR, A.G. & BRUNTON, S.L. 2016 Network structure of two-dimensional decaying isotropic turbulence. *J. Fluid Mech.* **795**, R2.

TAKAGI, K., GOTODA, H., TOKUDA, I.T. & MIYANO, T. 2017 Nonlinear dynamics of a buoyancy-induced turbulent fire. *Phys. Rev.* E **96**, 052223.

WALEFFE, F. 1997 On a self-sustaining process in shear flows. *Phys. Fluids* **9** (4), 883–900.

WANG, Y.X., CHOI, K.-S., GASTER, M., ATKIN, C., BORODULIN, V. & KACHANOV, Y. 2022 Opposition control of turbulent spots. *J. Fluid Mech.* **943**, A3.

WECK, P.J., SCHAFFNER, D.A., BROWN, M.R. & WICKS, R.T. 2015 Permutation entropy and statistical complexity analysis of turbulence in laboratory plasmas and the solar wind. *Phys. Rev.* E **91**, 023101.

WILLMARTH, W.W. & LU, S.S. 1972 Structure of the Reynolds stress near the wall. *J. Fluid Mech.* **55**, 65–92.

ZHANG, J. & SMALL, M. 2006 Complex network from pseudoperiodic time series: topology versus dynamics. *Phys. Rev. Lett.* **96**, 238701.

ZHANG, J., ZHOU, J., TANG, M., GUO, H., SMALL, M. & ZOU, Y. 2017*a* Constructing ordinal partition transition networks from multivariate time series. *Sci. Rep.* **7**, 7795.

ZHANG, W., LIU, P., GUO, H. & WANG, J. 2017*b* Detecting the chaotic nature in a transitional boundary layer using symbolic information-theory quantifiers. *Phys. Rev.* E **96**, 052215.

ZUNINO, L. & RIBEIRO, H.V. 2016 Discriminating image textures with the multiscale two-dimensional complexity-entropy causality plane. *Chaos Solitons Fractals* **91**, 679–688.

ZUNINO, L., SORIANO, M.C. & ROSSO, O.A. 2012 Distinguishing chaotic and stochastic dynamics from time series by using a multiscale symbolic approach. *Phys. Rev.* E **86**, 046210.